To appear in:
International Journal of Nano Dimension (Int. J. Nano Dimens.)

Online ISSN: 2228-5059 Print ISSN: 2008-8868

Dates:
Received: 12 January 2025
Revised: 29 September 2025
Accepted: 16 October 2025

DOI: https://doi.org/10.57647/ijnd.2026.1703.03

RSM-CCD Optimized EDTA-functionalized Magnetic Activated Carbon Derived from Sunflower Stem for Adsorptive Removal of Ni^{2+} and Malachite Green from Containment Water

Elham Fraid Aghazadeh[1], Mortaza Mirzaei*, [1], Akbar Hassanpour, [2], Ali Khani[1], Nader Jafarzadeh[1]**

[1]Department of Chemistry, Mi.C., Islamic Azad University, Miyaneh, Iran
[2] Department of Chemistry, Mara.C., Islamic Azad University, Marand, Iran

Corresponding Authors:

***Email Adderse:** mortazamirzaei_iau@iau.ir

****Email Adderse:** hassanpour78@iau.ir

Abstract

The structure of malachite green (MG) molecules makes them highly resistant to environmental degradation, posing significant challenges for removal. Similarly, heavy metals such as Ni^{2+} present substantial risks due to their toxicity and persistence. The presence of MG and Ni^{2+} in water and wastewater is frequently reported at levels exceeding standard limits, highlighting the urgent need for effective removal and degradation strategies. Herein, EDTA-functionalized magnetic activated carbon (EDTA-FMAC) derived from sunflower stems was developed and successfully applied for the removal of MG and Ni^{2+} from contaminated water. The adsorbent (MAC) was characterized using FTIR, XRD, SEM, Raman, VSM, and BET techniques. Key factors, including sorbent weight, contact time, initial pollutant concentration, and pH, were optimized using Response Surface Methodology (RSM). The study achieved maximum adsorption efficiencies of 97.68% for MG and 94.63% for Ni^{2+} at initial concentrations of 15 and 20 mg/L, adsorbent weights of 9 and 20 g, contact times of 25 and 20 minutes, and pH levels of 6 and 4, respectively. The experimental data aligned closely with the Freundlich isotherm model and the pseudo-second-order kinetic model. Thermodynamic analysis indicated that MG and Ni^{2+} adsorption onto magnetic activated carbon is endothermic and spontaneous. This study demonstrates that EDTA-functionalized magnetic activated carbon derived from sunflower stems is an efficient, effective, and reusable adsorbent for the removal of MG and Ni^{2+} from tap water.

Keyword: *Adsorption; Functionalized activated carbon; Heavy metals; Magnetic activated carbon; Malachite green.*

Introduction

Nickel, a toxic heavy metal, is widely used in various manufacturing sectors, including metal plating, galvanizing, smelting, mining, pigment production, and ceramics. Consequently, it is frequently found in industrial effluents [1-6]. This non-biodegradable metal has a high potential for accumulation in microorganisms, potentially leading to dermatitis and allergic reactions [7]. At higher concentrations, nickel is a potent carcinogen, associated with cancers of the lungs, nose, and bones [8-10]. With a *pKa of* approximately 9.86 for its hydrated form, Ni^{2+} remains in its cationic state under acidic to near-neutral pH conditions, which supports its mobility and availability for adsorption. Therefore, the removal of nickel from industrial effluents is crucial [11].

In parallel, environmental concerns also extend to malachite green (MG), a cationic dye widely used in various industrial sectors as a coloring agent. MG is released into water during its synthesis and application processes [12]. With a *pKa* of approximately 6.9, it primarily exists in its protonated cationic form under typical environmental pH conditions. Known for its toxicity and carcinogenicity, MG can cause skin irritation, allergies, and cancer in humans, underscoring the urgent need for its removal from water sources [13, 14].

To date, numerous techniques have been employed to purify polluted water and remove metal ions and dyes, including electrochemical methods, chemical precipitation, membrane filtration, ion exchange, and adsorption [12, 15, 16]. Among the diverse purification techniques, adsorption has emerged as one of the most reliable and technically feasible approaches due to its simplicity, ease of preparation and application, reproducibility, and cost-effectiveness [17, 18]. Common adsorbents include activated carbon, zeolites, chitosan, graphene, polymer materials, and clay. However, despite these advances, a critical gap remains: few studies have successfully developed a sustainable adsorbent that combines dual-function pollutant removal, high reusability, and magnetic separability using an eco-friendly synthesis route [19, 20]. As a result, there is a pressing need to develop versatile, high-capacity adsorbents capable of treating diverse pollutants in contaminated water. Addressing this challenge is critical for many countries facing serious water pollution issues [21, 22].

The use of activated carbon (AC) for heavy metal adsorption offers numerous advantages, including high adsorption capacity, effective metal recovery, excellent selectivity, sludge-free operation, and cost-effectiveness [23, 24]. However, the widespread application of commercial activated carbon is limited due to its production from expensive and non-renewable sources such as oil residues, wood, coal, and peat [25]. Recently, there have been advances in using abundant agricultural waste as a renewable, cost-effective alternative, rich surface functional groups and abundant inorganic mineral for AC production [26, 27]. Sunflower, extensively cultivated across many countries, generates significant waste in the form of stems [28]. These stems, primarily composed of carbonaceous compounds (40-50% cellulose, 20-30% hemicellulose, and 15-20% lignin), have been identified as excellent precursors for producing activated carbon [29]. Several studies have demonstrated the successful production of inexpensive and efficient powdered and granular activated carbon from sunflower stems through chemical activation methods [30, 31]. The resulting activated carbon exhibits a high surface area and porous structure, making it suitable for various applications, including wastewater treatment, water purification, and air filtration technologies [32]. However, one of the key challenges is the hydrophobic nature of activated carbon, which hinders its performance in water purification. To address this issue, chemical surface modification is often necessary. The addition of hydroxyl or carbonyl functional groups can enhance the hydrophilicity of activated carbon. Furthermore, inducing magnetic properties is an effective strategy to improve adsorption capacity, efficiency, and facilitate the easy separation of the adsorbent from water sources [33-36].

Ethylenediamine tetraacetic acid (EDTA), a polycarboxylic amino acid, has a strong ability to form stable chelates with metal ions and is considered a cost-effective material, making it widely used for modifying various substances. One of the key advantages of applying EDTA to different materials is its ability to enhance the adsorption of metal ions. However, research indicates that the adsorption capacity of EDTA-modified materials is significantly influenced by the type of substrate used [37, 38]. Among the various substrates, activated carbon (AC) stands out due to its unique properties, making it a highly effective and widely used adsorbent [39].

Fe_3O_4 nanoparticles are widely recognized as effective magnetic materials due to their simple preparation process and excellent biocompatibility. The magnetization of activated carbon (AC) sheets with Fe_3O_4 nanoparticles has driven the development of magnetic adsorbents for pollutant removal [40, 41].

To address this gap, the present work aims to develop a cost-effective, reusable, and magnetically responsive bio-based adsorbent capable of efficiently removing both Ni^{2+} and MG from wastewater. The AC was subsequently magnetized and functionalized with EDTA, serving as a chelating agent. The morphology, structure, and magnetic properties of the synthesized EDTA-functionalized magnetic activated carbon (EDTA-FMAC) were characterized through various analyses. The adsorption capacity of EDTA-FMAC for Ni^{2+} and MG was investigated. Additionally, the reproducibility and reusability of EDTA-FMAC were evaluated, demonstrating that the material is an efficient, stable, and reusable adsorbent for the removal of Ni^{2+} and MG from contaminated water. While some adsorbents reported in the literature exhibit high adsorption capacities such as banana peel-derived biosorbents (388.9 mg/g) [42], CNT/alumina composites (229.9 mg/g) [43], and Na-P1 zeolites (416.6 mg/g) [44] these materials often involve complex synthesis methods or limited reusability. Similarly, bottom ash achieved a malachite green adsorption capacity of 173.9 mg/g [45], though its recovery from aqueous systems remains challenging. In comparison, the EDTA-FMAC developed in this work displayed excellent adsorption capacities of 157.72 mg/g for Ni^{2+} and 162.80 mg/g for MG under optimized conditions. Although numerically slightly lower, these values were achieved using an abundant agricultural waste source, through a straightforward and eco-friendly functionalization route. The material demonstrated not only high dual-function adsorption performance but also magnetic separability and superior reusability, making it a compelling, scalable candidate for real-world wastewater treatment applications. This study addresses the critical need for sustainable and multifunctional adsorbents by developing a bio-derived material capable of removing both heavy metals and dyes from wastewater. The main objective is to synthesize and characterize an EDTA-functionalized, magnetically separable activated carbon from sunflower stem waste, and to evaluate its adsorption performance, reusability, and stability. This work not only contributes to the advancement of green adsorbent materials but also opens avenues for cost-effective and scalable solutions in environmental remediation, with potential applications in industrial-scale water treatment systems.

2. Experimental

2.1 Materials

All chemicals used in this study were of analytical grade and used without further purification. Ammonia solution 25% (M/s Merck, Germany), ethanol 96% (M/s Kimia Alcohol Zanjan, Iran), iron(II) sulfate heptahydrate (M/s Merck, Germany), ethylenediamine tetraacetic acid (EDTA) (M/s Merck, Germany), sodium hydroxide (M/s Kian Kave Azma, Iran), malachite green dye (M/s Merck, Germany), and nickel(II) nitrate 99.5% (M/s Merck, Germany) were purchased and used as received. Sunflower stems were collected from farms in Sufiyan (Tabriz, Iran). Potassium hydroxide, additional sodium hydroxide, acetic acid 96% (all from M/s Merck, Germany), and ferric chloride hexahydrate (M/s Sigma-Aldrich) were also employed in this research.

2.2 Instruments

The FT-IR spectrophotometer (Tensor 27, Bruker) was used to record the spectra by KBr pellets. X-ray diffraction (XRD) measurements were performed at room temperature by a Siemens diffractometer using Cu-Kα radiation at 35 kV in the scan range of 2θ from 5 to 80° (Tongda, TD-3700). UV–Vis absorption spectra were performed on a Shimadzu 1700 Model UV–Vis spectrophotometer. scanning electron microscopy (SEM) (MIRA3 FEG-SEM Tescan, Czech) was used for analyzing morphology of samples and the magnetization behavior was measured by the magnetometer (VSM, model MDKF, Iran).

Raman spectrum was determined by trchnooran company instrument (model Ram-532-004) in 532 nanometer wavelength.

2.3. Synthesis of sunflower stems based activated carbon

The creation of activated carbons from sunflower stem materials involves a two-step process; it starts with carbonization at low temperatures (700–800 K) in an oxygen-free environment to remove volatile substances, followed by activation at higher temperatures (1100–1300 ºK) to enhance the porosity and surface area of the resulting solid. In this study Sunflower stems were cut into small pieces and dried on oven at 100 °C, then it was crushed as a uniform powder, the obtained powder was ground and screened to collect average size of AC particles. Then the activating agents KOH were added to the powder. For this purpose, 1.5 grams of powder was soaked in 20 ml of 30% KOH. (The ratio of active carbon to the base was 1:3) it was stirred for 10 hours at room temperature. The activation process was carried out in a vacuum oven at 700 °C for 1 hour at 10 °C/min. Then, the activated carbon was dried after washing several time with ethanol: water, to reach the neutral pH range. Finally, the sunflower stem-based activated carbon (SSAC) was dried in an oven at 80 °C to obtain the product [46, 47]

2.4. Magnetization of sunflower stems based activated carbon

The co-participation method was employed to synthesize Magnetite Activated Carbon (MAC) nanocomposite. To initiate the magnetization process, 2.5 g of activated carbon obtained previous method was combined with 500 ml of distilled water and ultra-sonicated while 1 g of $FeCl_3 \cdot 6H_2O$ and 0.4 g of $FeSO_4 \cdot 7H_2O$ were added at a temperature of 80 °C. Ammonia solution was then added dropwise to adjust the pH to 9, The mixture was stirred in an inert environment at 60 °C for 2 hours to allow for deoxygenation. Following this, the solid particles were magnetically separated, rinsed three times with a 1:1 solution of water: ethanol, and ultimately dried at 60 °C for 24 hours [48, 49].

$$FeSO_4 + 2FeCl_3 + 8NH_4OH^- \rightarrow Fe_3O_4 + 6NH_4Cl + (NH_2)_2\ SO_4 + 4H_2O$$

2.5. EDTA- functionalized sunflower stems based activated carbon

To prepare the EDTA-FMAC adsorption, 4.5 g of EDTA and 3 g of NaOH were mixed with the magnetic activated carbon obtained from the previous step in 150 ml of distilled water. The mixture was stirred uniformly at ambient temperature for 24 hours. Afterward, the resulting suspension was washed with a 1:1 ratio of ethanol and distilled water. Finally, the mixture was dried at 60 °C [50, 51].

2.6. Adsorption studies

Adsorption and isotherms were investigated by conducting batch experiments and analyzing via AAS instrument. The adsorption capacity at equilibrium (qe, mg/g), and the percentage removal (Removal, %) can be calculated by the following equations:

$$q_e = \frac{(C_0 - C_e)V}{m}$$

$$\text{Removal\%} = \frac{C_0 - C_e}{C_0} \times 100$$

Where q_e is the adsorption capacity (mg/g), C_o (mg/L) and C_e (mg/L) are the initial and equilibrated concentrations, respectively, V (L) is the volume of solution added, and m (g) is the mass of the adsorbent [52].

2.7. Optimization of the adsorption process of Ni^{2+} and MG via RSM

In this study, RSM, the Central Composite design method (CCD), is used to optimize the absorption process for the removal of Ni^{2+} ions and MG. Four effective Factors in the process of Ni^{2+} ions and MG removal, including the initial concentration of Ni^{2+} and MG (mg/l), the initial pH of the Ni^{2+} and MG solution, the absorption time (min) of Ni^{2+} and MG, and the adsorbent weight (mg) were investigated

(**Table 1**). 31 experiments were proposed by Design Expert 11, which included 6 repetitions at the central point. The following second-order multi-order equation was used to connect between dependent and non-dependent variables:

$$Y = \beta_\circ + \sum_{i=1}^{k} \beta_i X_i + \sum_{i=1}^{K} \beta_{ii} X_i^2 + \sum_{1 \le i \le j}^{k} \beta_{ij} X_i X_j + \varepsilon$$

where (Y) represents the adsorption efficiency, Xi and Xj denote the experimental levels of variables, (βi) stands for the linear correlation coefficient, (βii) indicates the second-order correlation, (βij) signifies the cross-correlation coefficient, and (ε) represents the random error. The variables i, j, and k correspond to the number of variables under analysis.

Table 1. Range of parameters and levels of test variables for Pb^{2+} removal.

Variable	**levels**				
	-2	**-1**	**0**	**1**	**2**
Ni^{2+} Concentration (X_1)	5	10	15	20	25
Initial pH (X_2)	3	5	7	9	11
Adsorbent weight (X_3)	3	5	7	9	11
time (X_4)	5	15	25	35	45

2.8 Adsorption isotherms and reaction kinetics studies

Adsorption behavior is commonly interpreted using theoretical models that describe both equilibrium and kinetic aspects of the process. Isotherm models such as Langmuir and Freundlich are used to characterize the interaction between adsorbate molecules and the surface of the adsorbent. These models help determine whether adsorption occurs as a monolayer on a homogeneous surface or as multilayer coverage on heterogeneous sites. Kinetic models, including pseudo-first-order and pseudo-second-order equations, are employed to evaluate the rate and mechanism of adsorption, indicating whether the process is governed by physical diffusion or chemical interaction. The linear forms of these models, along with their corresponding plotting formats, are summarized in **Table 2**. These equations provide the basis for analyzing experimental data and optimizing adsorption systems for practical applications.

Table.2 Scientific principles and modeling approaches in adsorption studies.

Kinetic Models	Linear form	Plot
Pseudo-first order	$\frac{dq_t}{dt} = K_1(q_e - q_t)$	$\log(q_e - q_t) = logq_e - \frac{K_1}{2.303}t$
Pseudo-second order	$\frac{dq_t}{dt} = K_2(q_e - q_t)^2$	$\frac{t}{q_t} = \frac{1}{k_2 q_e^2} + \frac{1}{q_e}t$
Isotherm Models	**Linear form**	**Plot**
Langmuir	$q_e = \frac{c_e k_l q_m}{1 + c_e k_l}$	$\frac{c_e}{q_e} = \frac{1}{k_l q_m} + \frac{c_e}{q_m}$
Freundlich	$q_e = K_f C_e^{\frac{1}{2}}$	$logq_e = \frac{1}{n} logC_e + logK_f$

Where k_1 and k_2 represent the rate constants for the pseudo-first-order and pseudo-second-order kinetic models, respectively (h^{-1}). The terms q_e and q_t denote the amount of adsorbate retained by the adsorbent at equilibrium and at a given time t, respectively, both expressed in mg/g. The variable C_e refers to the equilibrium concentration of the contaminant in solution (mg/L), while q_m indicates the theoretical maximum adsorption capacity under equilibrium conditions (mg/g). The Langmuir constant K_L is associated with the affinity of binding sites and the energy of adsorption. In the Freundlich model, K_F and $1/n_l/n$ are empirical constants that reflect the adsorption capacity (mg/g) and the intensity or favorability of the adsorption process, respectively.

3. Results and discussion

3.1 Characterization

Fig. 1 exhibits FT-IR spectra of AC, MAC and EDTA F-MAC derivatives presented from bottom to top. A sharp peak observed at 3435.98, 3431.46 and 3426.65 cm^{-1} is related to stretching vibration of OH functional group (3200-3500 cm^{-1}) respectively which assigns OH stretching vibration of phenols and water molecules. Distinct peaks at 2920.94, 2924.81 and 2922.28 cm^{-1} represent aliphatic stretching vibration related to CH_2 group (2800-3000 cm^{-1}). The sharp peak at 1639.21, 1643.81, and 1642.4 cm^{-1} is attributed to the carbonyl (C=O) functional group (1600–1650 cm^{-1}). The Fe–O stretching vibration peak for MAC appears at 581.73 cm^{-1}, which shifts to 557.36 cm^{-1} in EDTA-FMAC due to the carbonization effect. A distinct peak observed at 1061.48, 1025.12, and 1023.35 cm^{-1} corresponds to the C–O stretching vibration (1018–1149 cm^{-1}). These characteristic peaks confirm the successful synthesis and accuracy of the adsorbent [53-55].

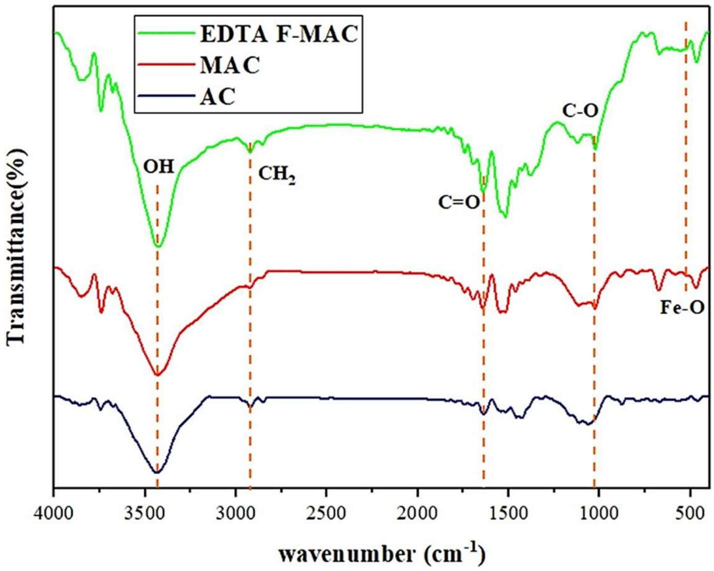

Fig. 1: The FTIR spectrum of EDTA F-MAC, MAC and AC.

Fig. 2 presents the Raman spectra of AC sample, MAC and EDTA F-MAC, respectively. All of samples display common broad peaks approximately at 1320-1340 and 1580-1590 cm$^{-1,}$ corresponding to D bond and G bond. G bond indicates sp^2 C-C in-plane vibrations and graphite lattice. D bond exhibits sp^3 structural defects which show disorders of active sites. I_D/I_G is a ratio for representing structures disorder in graphitic materials [56, 57]. This ratio for AC, MAC and EDTA F-MAC is 1.01, 1.03 and 1.04 which claims enhancement the defects of modified AC adsorbent leading to increase the active sites for removal of pollutants. Three peaks at 214, 284 and 398 cm^{-1} for Fe_3O_4 were identified in MAC spectra. 214 and 284 were considered to E_g and T_{2g} asymmetric modes and 398 was corresponded to A_{1g} mode [58, 59].

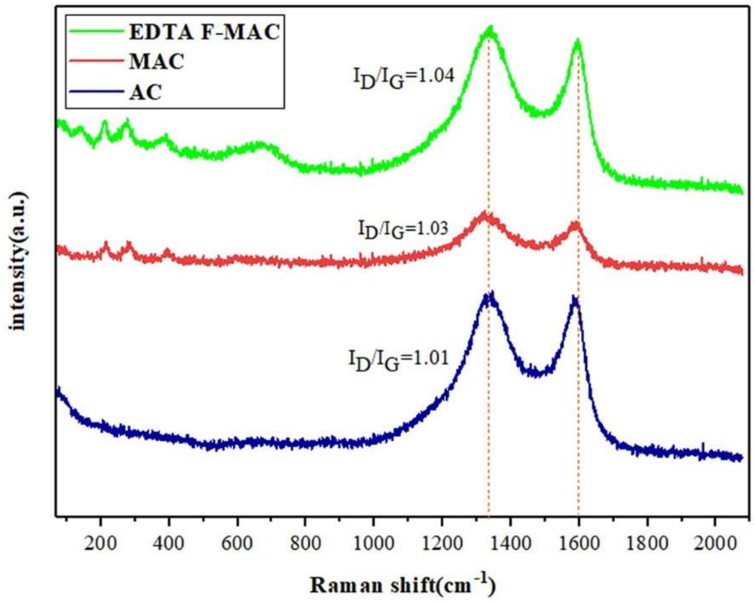

Fig. 2: The raman shift of EDTA F-MAC.

XRD analysis is one of the best techniques to identify the crystallinity or amorphous structure of ACs derived materials. The **Fig. 3** shows XRD graph of AC which exhibits 2 sharp peaks at around 2θ=26.8° and 2θ=44.7° corresponding to (002) and (101) planes for thick layers of carbon-containing structure. These peaks demonstrate the effect of employed temperature for activation of AC which lead to formation of the partial graphitic structure at amorphous AC. According to JCPDS card (JCPDS-19-0629) analysis of MAC in comparison with AC exhibits diffraction peaks related to (311), (400), (440) cubic crystal planes of Fe_3O_4 penetrating to AC structure. The diffraction peak at around 2θ=17.02° probably is related to EDTA structure [60, 61].

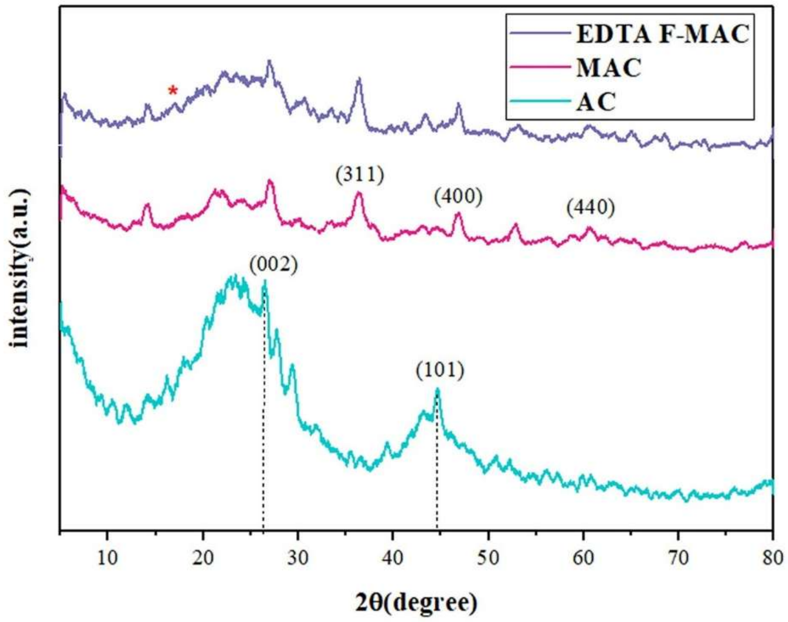

Fig. 3: The XRD pattern of EDTA F-MAC, MAC and AC.

The FESEM analysis is an appropriate method to illustrate the morphological details of MAC and EDTA-functionalized MAC, as shown in **Fig. 4**. Figures (**4a**, **4b**) depict a relatively smooth structure with some pores and surface wrinkles on the MAC. After the functionalization process with EDTA, it is evident that EDTA is well-dispersed within the MAC, leading to significant changes in the heterogeneous structure and porosity. This modification results in spherical agglomeration of particles, enhancing the porous structure and improving the adsorbent properties [62-64].

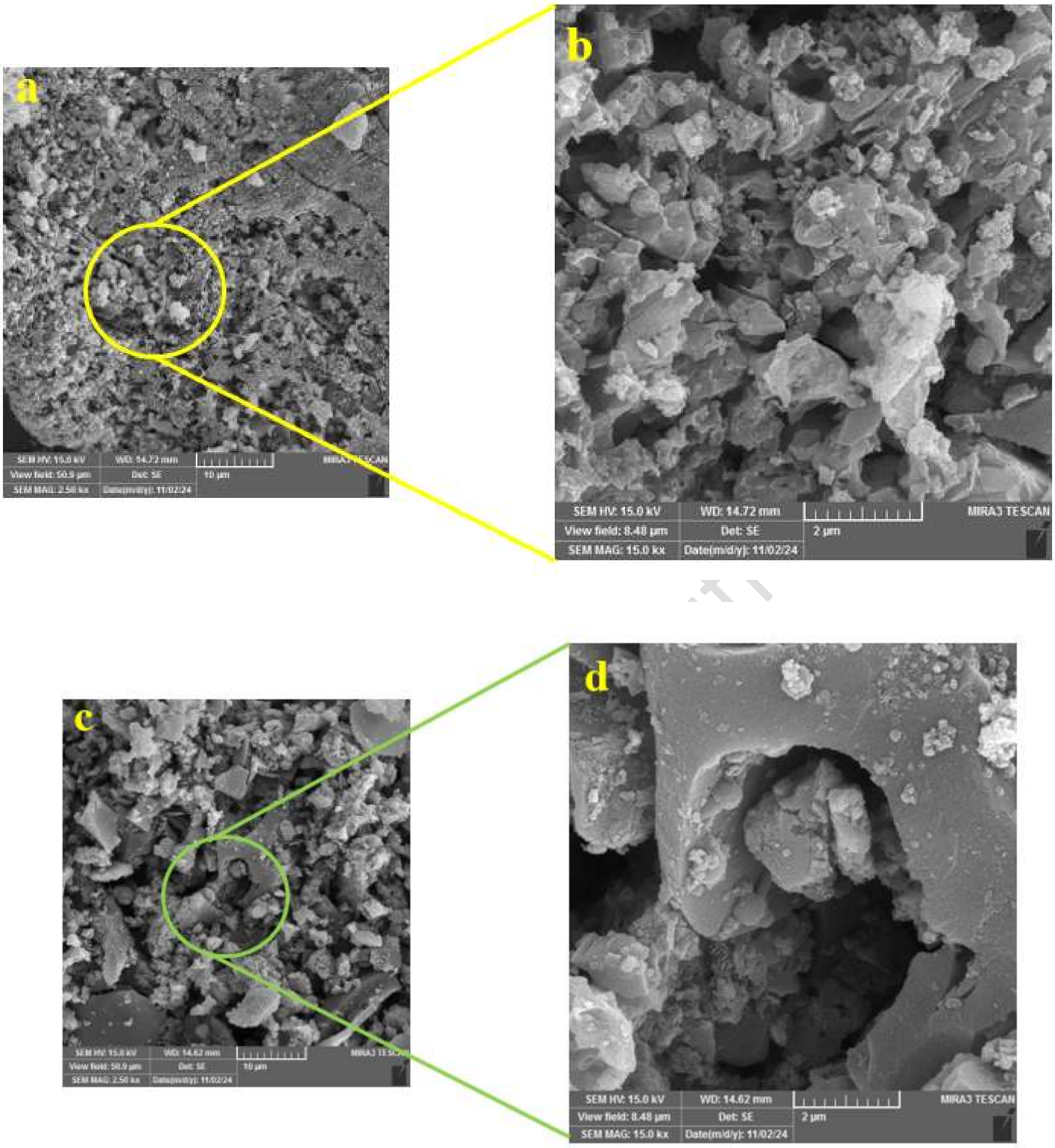

Fig. 4: The SEM images of MAC and EDTA F-MAC.

Fig. 5 shows the N_2 adsorption-desorption isotherm for the EDTA F-MAC adsorbent. The graph is classified as a type I isotherm, indicating the presence of two-dimensional slit pores. The incorporation of Fe_3O_4 particles into the AC pores, along with EDTA within the MAC structure, reduces N_2 adsorption capacity. Noticeable values like a_s, V_m and total pore volume are 146.85 m^2/g, 33.739 cm^3/g and 0.1333

cm^3/g, respectively. Additionally, **fig. 6** presents the pore volume distribution of the synthesized adsorbent. The peak pore radius (r_p) for EDTA F-MAC is 1.21 nm, indicating a microporous structure (< 2 nm). This microporosity plays a significant role in the sharp increase in N_2 adsorption [65, 66].

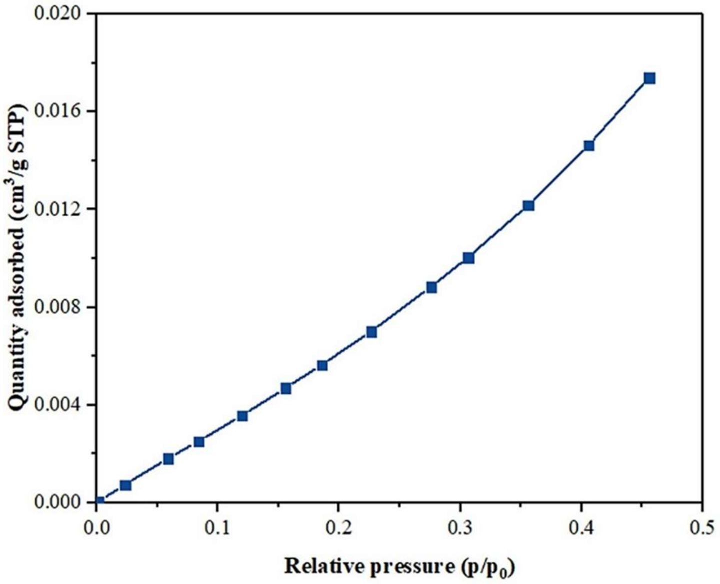

Fig. 5: N_2 adsorption-desorption isotherm for EDTA F-MAC.

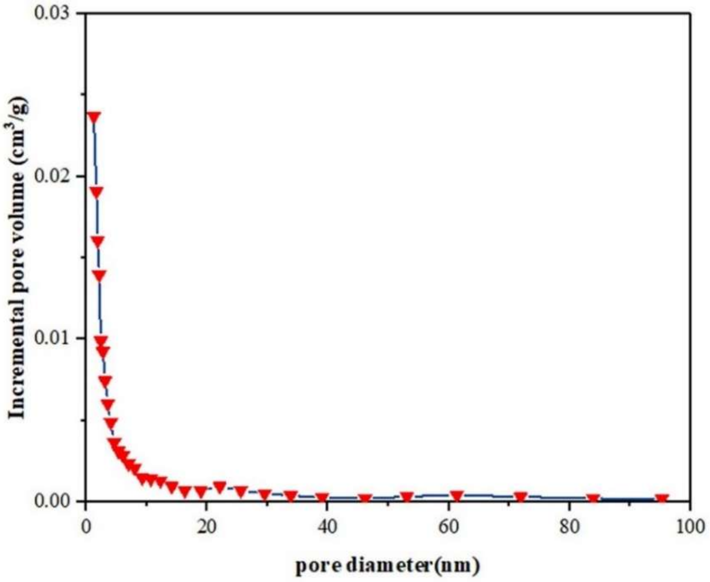

Fig. 6: Pore volume distribution of EDTA F-MAC.

The magnetic property versus applied magnetic field of EDTA F-MAC is exhibited on **fig. 7**. The synthesized adsorbent, with a saturation magnetization (µs) of 8.15 emu/g, shows superparamagnetic characteristics. The sigmoidal curve and the ease of particle separation with a magnet highlight the adsorbent's suitability for use in aqueous solutions [67-69].

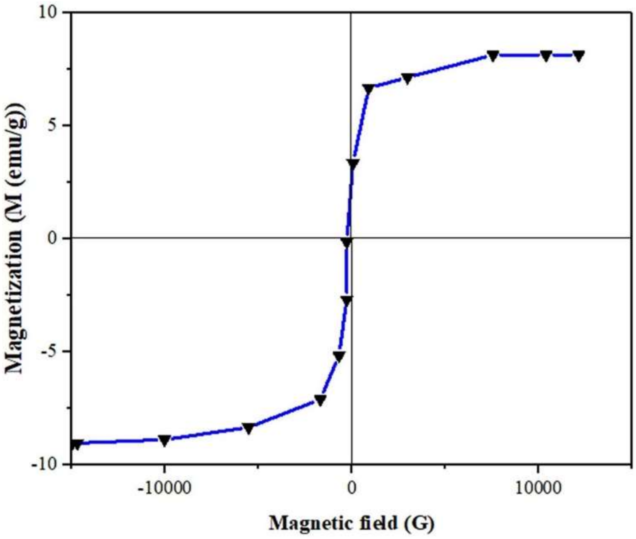

Fig.7: The magnetic property versus applied magnetic field of EDTA F-MAC.

3.2 Analysis of Variance (ANOVA)

Various RSM computations for the current optimization study were performed employing Design-Expert 11 software. A statistical second-order model, which includes interaction and polynomial terms, was developed for all response variables. The general form of the model is represented as in the following:

$$Y=73.29-5.8X_1-2.35X_2+3.96X_3X_4.65X_1X_2-2.27X_1X_3+4.81X_2X_3$$

$$Y=76.28-0.91X_1-1.96X_2-3.27X_3+9.61X_4-1.07X_1X_3+1.90X_2X_3-1.69X_2X_4-0.69X_3X_4+0.69X_4^2$$

These equations represent the statistical model, where Y is the response variable and X_1, X_2, X_3, and X_4 are the independent variables. The model includes both interaction and polynomial terms to analyze the complex interactions between the independent variables and their effects on the response variable.

Coefficients of the variables (e.g., -5.8X_1 and 3.96X_3X_4) indicate the influence of each variable on the final response. Interaction terms (such as X_1X_2 and X_2X_3) reflect the combined effects of two or more independent variables on the response variable. Using such advanced statistical models allows for a precise analysis of the individual and interactive effects of independent variables on the response, helping to optimize the study's results. **Table 2** presents both the experimental data and the results derived from the model equations. The findings demonstrate that this model accurately represents the experimental outcomes and is effective in predicting the output variable under various conditions. A comparison between the experimental results for the adsorption efficiency of Ni^{2+} and MG and the RSM model outcomes shows a significant overlap, as visually represented in **figs. 8a** and **8b.** Additionally, the ANOVA results are provided in **table 3**. Based on these results, the proposed model is identified as quadratic.

Table 2: Experimental and RSM predicted results for Ni^{2+} adsorption.

	Factor 1	**Factor 2**	**Factor 3**	**Factor 4**	**Response 1**	**Response 2**
Run	**A:pH**	**B:Pollutant Concentration**	**C:Adsorbent weight**	**D:time**	**Ni**	**MG**
1	4	20	6	10	82.23	66.67
2	6	5	9	15	78.25	80.32
3	6	15	9	25	81.19	97.68
4	4	20	6	20	80.22	85.47
5	8	20	6	20	46.31	86.45
6	8	10	6	20	70.1	95.64
7	8	10	12	20	80.65	83.29
8	8	10	6	10	80.62	72.26
9	4	20	12	10	70.26	69.12
10	4	10	12	20	81.85	87.54
11	8	20	6	10	54.62	68.12
12	4	20	12	20	94.63	83.07
13	8	20	12	10	60.83	65.89
14	6	15	9	15	73.21	75.98
15	6	15	3	15	72.23	84.52
16	4	10	6	10	84.49	72.69
17	6	15	15	15	71.62	69.8
18	8	20	12	20	78.59	79.28
19	6	15	9	15	74.19	75.98
20	2	15	9	15	82.21	79.09
21	6	15	9	15	74.19	75.98
22	6	15	9	15	72.41	77
23	4	10	6	20	86.92	95.78
24	8	10	12	10	66.42	60.82
25	6	25	9	15	70.14	71.18
26	4	10	12	10	57.04	64.85
27	6	15	9	15	73.07	76.77

28	6	15	9	5	64.96	60.36
29	10	15	9	15	62.35	74.84
30	6	15	9	15	73.04	75.98

Table 3: ANOVA analysis of Ni^{2+} and MG removal.

Source of variations	**Regression**		**Adjusted R2**		**Predicted R2**		**F-value**		**Lack of Fit**		**Model**	
	R1	**R2**	**R1**	**R2**	**R1**	**R2**	**R1**	**R2**	**R1**	**R2**	**R1**	**R2**
	0.98	0.99	0.98	0.96	0.99	0.98	166.60	282.37	0.0517	0.0651	2FI	Quadratic

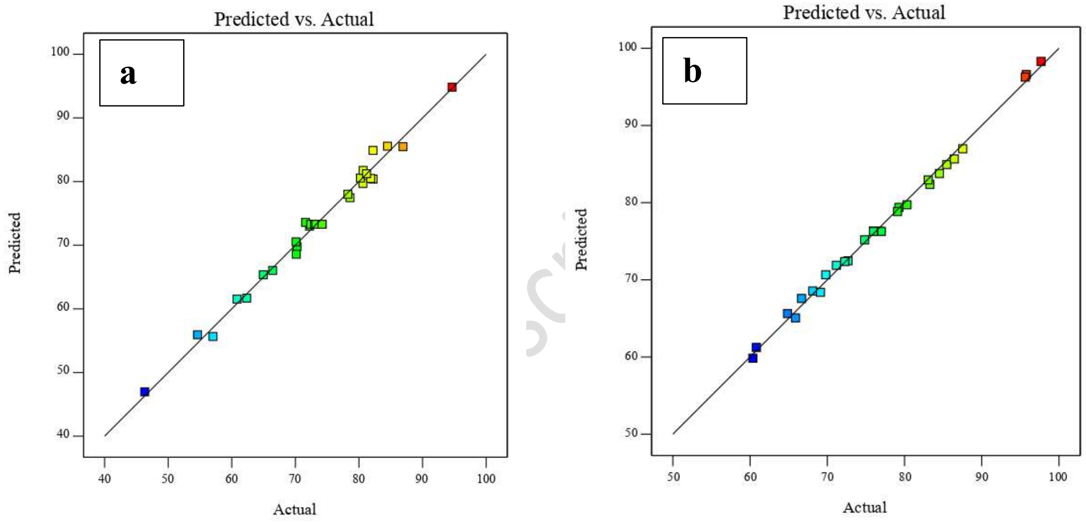

Fig. 8: Comparison of predicted and actual value for removal of a) Ni^{2+} and b) MG based on RSM results.

3.2.1 Effect of pH and Pollutant Concentration on Adsorption Efficiency and Point of Zero Charge (pHpzc)

To determine the point of zero charge (pHpzc) of the EDTA-FMAC adsorbent, a series of 50 mL solutions of 0.1 N $NaNO_3$ were prepared. The initial pH of each solution was adjusted to 2, 4, 6, 8, 10, and 12 using 0.1 N HCl or NaOH. Then, 40 mg of the adsorbent was added to each solution, and the suspensions were stirred at room temperature for 48 hours to ensure equilibrium. After equilibration, the final pH was measured, and the difference between final and initial pH (ΔpH) was calculated. The ΔpH values were plotted against the initial pH to determine the pHpzc. The point at which ΔpH = 0 was identified as the pHpzc, which was approximately 4.0 for Ni^{2+} and 6.5 for MG (**Figs. 9a and 9b**). The pH of the solution plays a crucial role in controlling the surface charge of the adsorbent and, consequently, the adsorption behavior of both Ni^{2+} and MG. At pH values below the pHpzc, the adsorbent surface becomes positively charged, which typically repels cationic species. However, Ni^{2+} adsorption is enhanced under acidic conditions (pH ≈ 4) due to strong chelation with the EDTA functional groups, which dominate over electrostatic repulsion. In contrast, MG adsorption is most efficient near pH 6.5, where the surface charge is neutral to slightly negative, allowing favorable interactions with the dye's aromatic rings and polar functional groups such as hydroxyl and carbonyl. A comparative analysis across the same pH range reveals distinct adsorption mechanisms for the two pollutants. Ni^{2+}, as a small divalent metal ion, is highly sensitive to electrostatic interactions and forms stable complexes with EDTA, leading to optimal adsorption at lower pH. MG, being a bulky organic dye, interacts primarily through π–π stacking and hydrogen bonding, which are favored near neutral pH. These differences in molecular structure and interaction pathways explain the observed variation in adsorption efficiency between Ni^{2+} and MG [70].

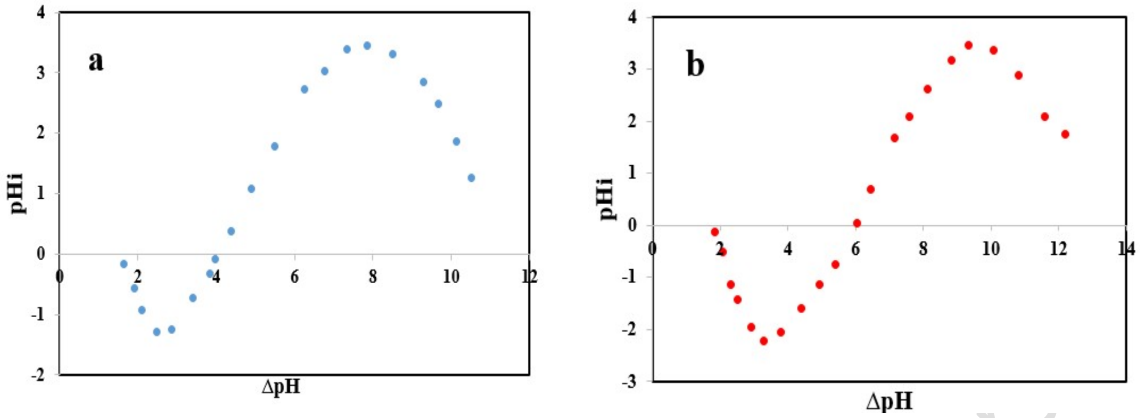

Fig. 9: Isoelectric point diagram of EDTA F-MAC for, a) Ni^{2+} and, b) MG adsorption.

The 3D graph for Ni^{2+} and MG removal based on RSM provided in **figures 10(A-L).** As shown in **fig. 10-A** (for Ni^{2+} removal) the efficiency initially increases with rising pH. However, beyond pH 6, the removal efficiency begins to decrease. This decline could be attributed to the formation of soluble complexes or other chemical interactions that negatively impact the Ni^{2+} removal process. At lower pH values, increasing the pollutant concentration appears to enhance removal efficiency. This could be due to the increased availability of adsorption sites or favorable chemical interactions at lower pH, which promote better adsorption of Ni^{2+}. For MG, as shown in **fig. 10-G**, lower pH and higher pollutant concentration lead to improved removal efficiency. Acidic conditions can enhance adsorption capacity, and a lower pollutant concentration reduces competition for adsorption sites, thus improving overall efficiency.

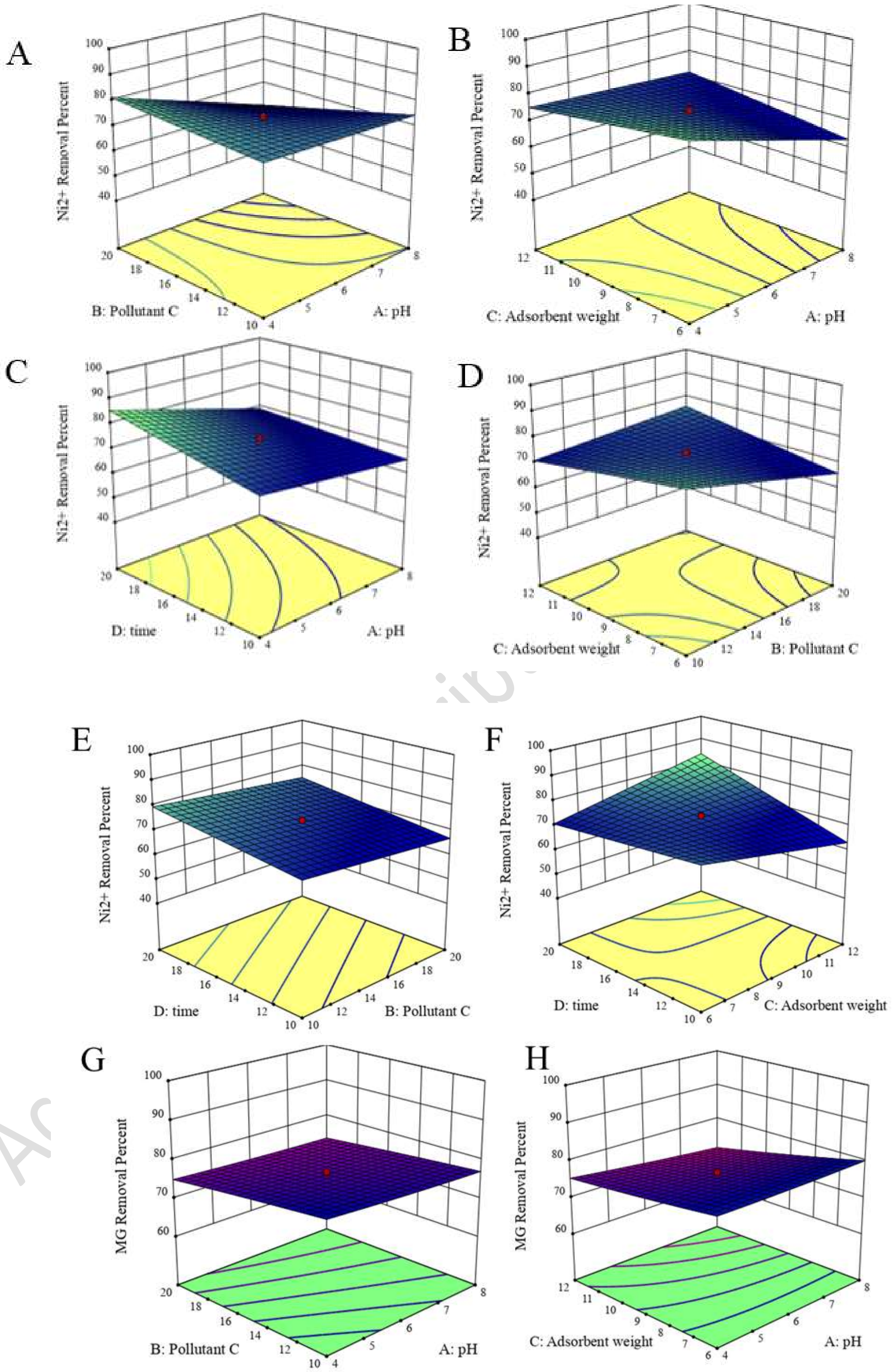
A
Ni2+ Removal Percent
100
90
80
70
60
50
40
B: Pollutant C
20
18
16
14
12
10
A: pH
4
5
6
7
8
B
Ni2+ Removal Percent
C: Adsorbent weight
12
11
10
9
8
7
6
A: pH
C
Ni2+ Removal Percent
D: time
A: pH
D
Ni2+ Removal Percent
C: Adsorbent weight
B: Pollutant C
E
Ni2+ Removal Percent
D: time
B: Pollutant C
F
Ni2+ Removal Percent
D: time
C: Adsorbent weight
G
MG Removal Percent
100
90
80
70
60
B: Pollutant C
A: pH
H
MG Removal Percent
C: Adsorbent weight
A: pH

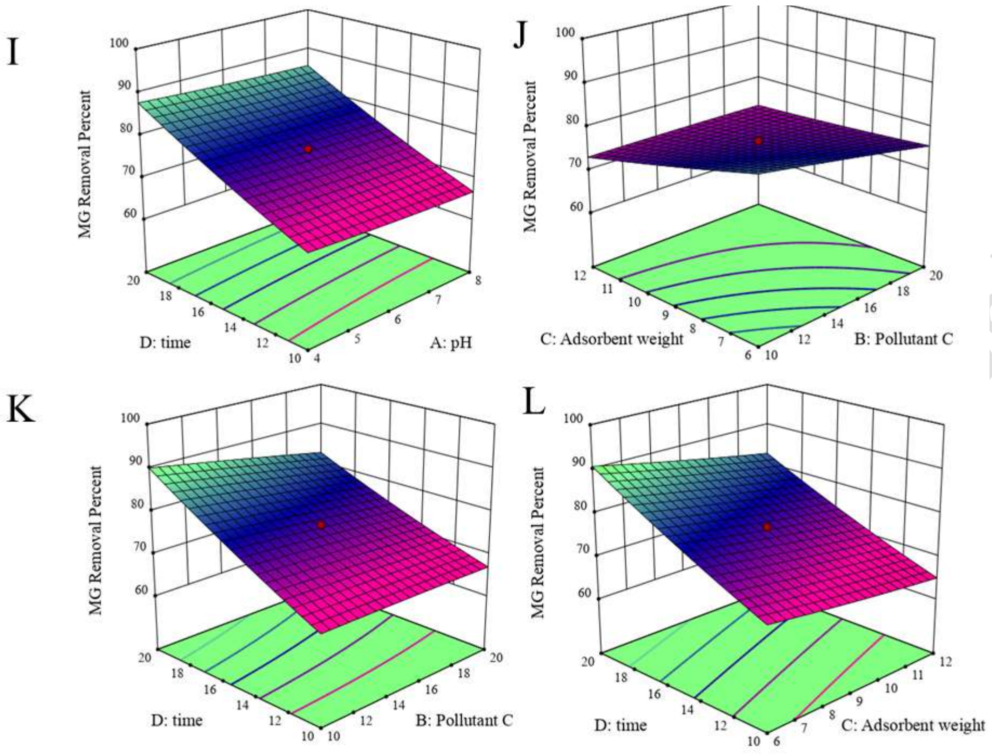

Fig.10 (A-L): The 3D graph for Ni^{2+} and MG removal based on RSM.

3.2.2. pH and adsorbent weight effect on adsorption efficiency

As shown in **fig. 10-B**, the interaction between pH and adsorbent weight significantly affects the removal efficiency of Ni^{2+}. Increasing the adsorbent weight at lower pH values leads to enhanced adsorption, primarily due to the greater availability of active sites and increased surface area. A higher dosage allows more pollutant molecules to interact with functional groups such as carboxyl and EDTA moieties, improving overall efficiency. At higher pH levels (above 6), the formation of nickel hydroxide species such as $Ni(OH)_2$ becomes dominant. These complexes are poorly soluble and tend to precipitate, reducing the concentration of free Ni^{2+} ions in solution. Since the adsorbent primarily interacts with ionic forms of nickel, the presence of hydroxide complexes inhibits adsorption. This phenomenon explains the observed decline in efficiency at elevated pH values. The 3D response surface plot (Fig. 10-B) illustrates this trend clearly: maximum adsorption occurs at low pH (≈4) and high adsorbent weight (≈12 mg). The curvature of the surface confirms a nonlinear relationship, where adsorption efficiency increases sharply with adsorbent dose at acidic pH but plateaus or declines at higher pH due to chemical speciation effects. A similar pattern is observed for MG adsorption **(fig. 10-H),** where increased adsorbent weight enhances removal, especially under mildly acidic to neutral conditions. This is attributed to improved interaction between dye molecules and surface functional groups, facilitated by higher surface area.

3.2.3. pH and time effect on adsorption efficiency

The interaction between pH and contact time significantly influences Ni^{2+} adsorption. As shown in **fig. 10-C**, adsorption efficiency increases more rapidly at lower pH values over time. This is due to stronger electrostatic attraction and chelation between Ni^{2+} ions and EDTA-functionalized sites on the adsorbent surface. At higher pH, the formation of $Ni(OH)_2$ complexes reduces the availability of free Ni^{2+} ions, slowing the adsorption process. To support this observation, kinetic data were fitted to three models. The pseudo-first-order plot **(fig. 11d)** yielded $R^2 = 0.9774$, indicating that the rate depends on the concentration of Ni^{2+}. The pseudo-second-order model **(Fig. 11e)** showed even stronger correlation ($R^2 = 0.9867$), suggesting chemisorption as the dominant mechanism. The intraparticle diffusion plot **(Fig. 11f)** revealed a multi-stage process, with initial surface adsorption followed by gradual pore diffusion.

3.2.4. Adsorbent weight and pollutant concentration effect on adsorption efficiency

As shown in Fig. **10-D**, the interaction between adsorbent dose and pollutant concentration significantly affects the adsorption performance. At lower concentrations, increasing the adsorbent dose leads to higher removal efficiency due to the abundance of active sites. However, as the pollutant concentration increases beyond a threshold, the surface of the adsorbent becomes saturated, and the efficiency begins to decline. This is attributed to the limited number of available binding sites, which cannot accommodate excess pollutant molecules. The 3D response surface plot illustrates this saturation effect clearly. A plateau is observed at high concentrations, indicating that the adsorbent has reached its maximum capacity. Optimal conditions are achieved at moderate pollutant concentrations (e.g., 50–75 mg/L) and higher adsorbent doses (e.g., 12–15 mg), where the balance between surface availability and pollutant load is favorable [71].

3.2.5. Time and pollutant concentration effect on adsorption efficiency

Fig. 10-E and Fig. **10-K** present the 3D response surface plots illustrating the combined effect of contact time and initial pollutant concentration on removal efficiency for Ni^{2+} and MG, respectively. The plots reveal a nonlinear interaction between these two variables. At lower pollutant concentrations (e.g., <50 mg/L), the adsorbent surface remains unsaturated, and increasing contact time allows more ions to diffuse and bind to available active sites, resulting in higher removal efficiency. As the initial concentration increases, the number of ions competing for adsorption sites rises sharply. Although the initial uptake may be rapid, the surface approaches saturation more quickly, and the efficiency plateaus or even declines despite extended contact time. This behavior is consistent with the pseudo-second-order kinetic model, where the rate of adsorption slows as equilibrium is approached. The curvature of the response surface confirms that maximum removal occurs under moderate concentrations and sufficient contact time. Beyond a certain concentration threshold, the adsorbent's capacity becomes limiting, and additional time yields diminishing returns. These trends highlight the importance of balancing pollutant load with contact duration to optimize adsorption performance.

3.2.6. Time and adsorbent weight effect on adsorption efficiency

Fig. 10-F and **Fig. 10-L** illustrate the combined effect of contact time and adsorbent dose on the removal efficiency of Ni^{2+} and MG, respectively. The response surface plots reveal a nonlinear relationship, where increasing both parameters generally enhances adsorption performance. A higher adsorbent dose provides more active sites for interaction, while a longer contact time allows sufficient diffusion and binding of pollutant molecules. However, this improvement is pH-dependent and does not occur uniformly across all conditions. At extreme pH values, particularly under alkaline conditions, the formation of hydroxide complexes and changes in surface charge can limit adsorption, even with increased dose and time. The

curvature of the plots indicates that maximum efficiency is achieved under mildly acidic to neutral conditions, beyond which the surface approaches saturation and further increases in time or dose yield minimal gains. These trends are consistent with pseudo-second-order kinetics, where rapid initial uptake is followed by a slower approach to equilibrium.

3.3. Adsorption isotherms, reaction kinetics and thermodynamic parameters study

Kinetic data provide valuable insights into the adsorption mechanism, which is essential for optimizing the efficiency of the adsorption process **(Figs 11a-f).** Understanding the adsorption rate is critical for effective heavy metal removal from water and for refining design parameters. The adsorption rate constant of Ni^{2+} on the EDTA F-MAC adsorbent was evaluated under specific conditions: an adsorbent weight of 16 mg, pH of 4, initial Ni^{2+} concentrations of 5, 10, 15, 20, 25, and 30 mg/L, and a test duration of 1 hour. An experiment was conducted to examine the reaction kinetics, and the collected data were used to construct plots for first-order (**Fig. 11a**), second-order (**Fig. 11b**), and intraparticle diffusion models (**Fig. 11c**). The correlation coefficients were compared, revealing that the adsorption reaction kinetics for EDTA F-MAC followed a first-order model. This indicates that the adsorption rate is directly proportional to the adsorbate concentration in the solution.

The adsorption data were further analysed using various isotherm models, including Langmuir (**Fig. 11d**), Freundlich (**Fig. 11e**), and Temkin (**Fig. 11f**). The results demonstrated the best fit with the Freundlich isotherm, suggesting that the adsorption process on EDTA F-MAC occurs in a multilayer manner over a heterogeneous surface. The value of 1/n obtained from the Freundlich model was between 0 and 1, confirming favorable adsorption and indicating surface heterogeneity. Although the Langmuir model was less accurate, it was used to estimate the monolayer adsorption capacity (q_{max}) for comparison purposes.

For the thermodynamic studies, solutions with Ni^{2+} concentrations of 15 and 9 mg/L were tested at temperatures of 25 and 45 °C, with contact times ranging from 1 to 25 minutes. Thermodynamic parameters including Gibbs free energy (ΔG), enthalpy change (ΔH), and entropy change (ΔS) were calculated using the following equations [72]:

$$lnK_c = \frac{\Delta S}{R} - \frac{\Delta H}{RT}$$

$$\Delta G = \Delta H - T\Delta S$$

$$\Delta G = -RTlnK_c$$

Here, R is the universal gas constant (8.314 J/mol. ºK), T is the absolute temperature in Kelvin, and Kc is the equilibrium constant derived from adsorption data. The negative values of ΔG at both temperatures confirm that the adsorption process is spontaneous. The positive ΔH value (4.715 kJ/mol) indicates that the process is endothermic, suggesting strong chemical interactions between Ni^{2+} ions and the EDTA-functionalized adsorbent. Additionally, the positive ΔS value (12.43 J/mol. ºK) reflects increased randomness at the solid–solution interface during adsorption [73].

Table 4. Thermodynamic parameters for EDTA F-MAC adsorbent.

ΔT(°C)	ΔG (KJ/mol)	ΔH (KJ/mol)	ΔS (J/K.mol)
25	-20.458	4.715	12.43
45	-16.405		

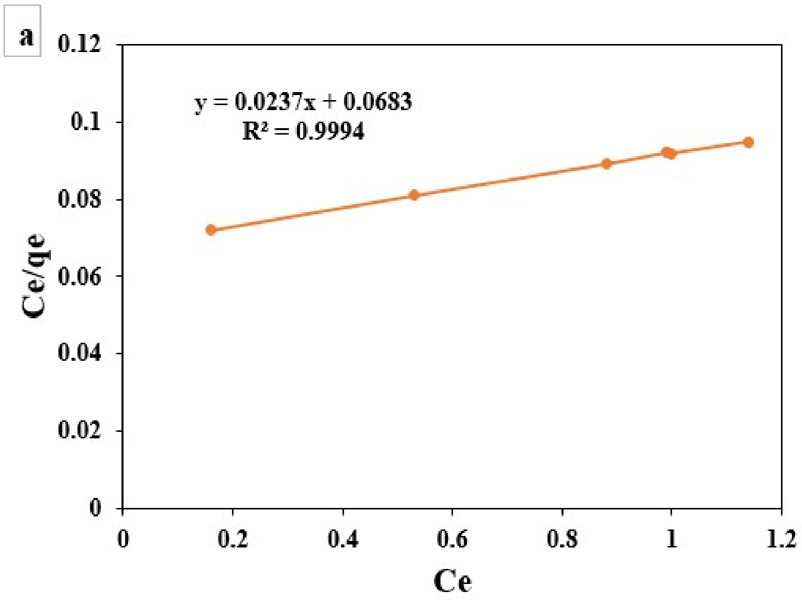

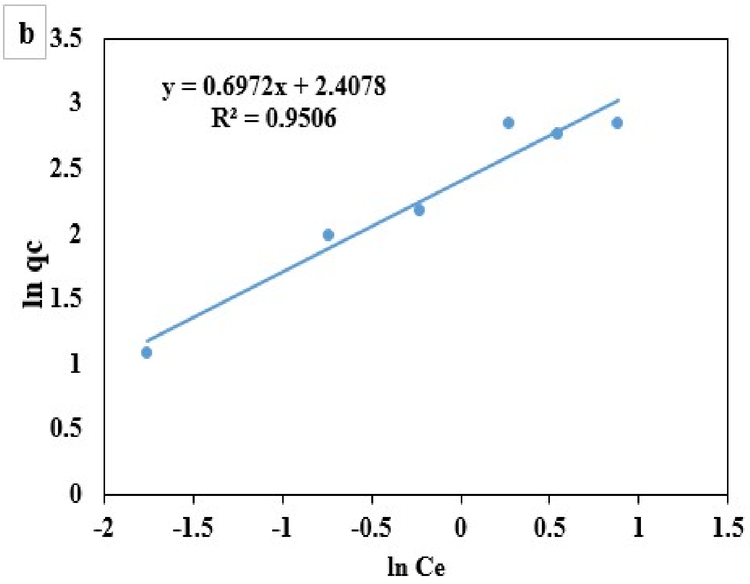
b
y = 0.6972x + 2.4078
R² = 0.9506
ln qc
ln Ce
3.5
3
2.5
2
1.5
1
0.5
0
-2
-1.5
-1
-0.5
0
0.5
1
1.5

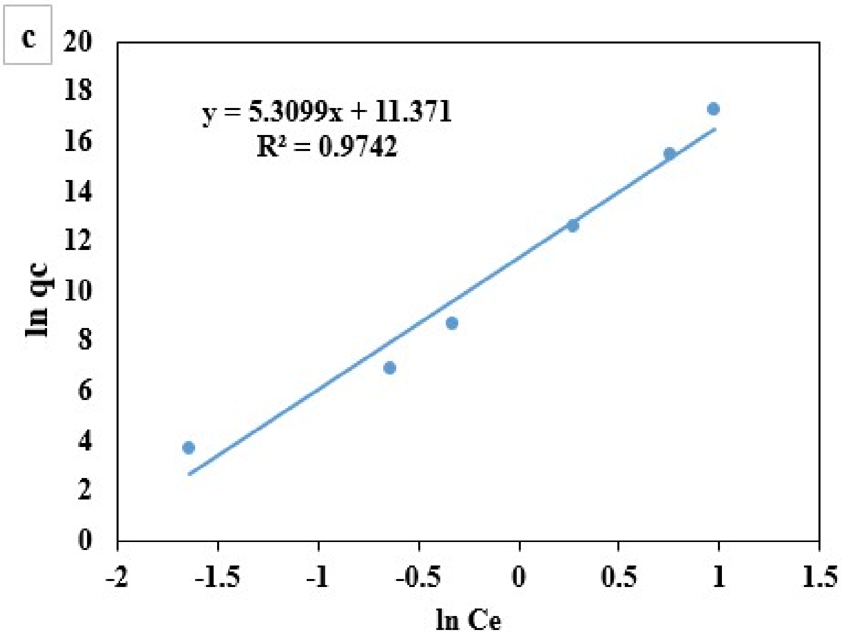
c
y = 5.3099x + 11.371
R² = 0.9742
ln qc
ln Ce
20
18
16
14
12
10
8
6
4
2
0
-2
-1.5
-1
-0.5
0
0.5
1
1.5

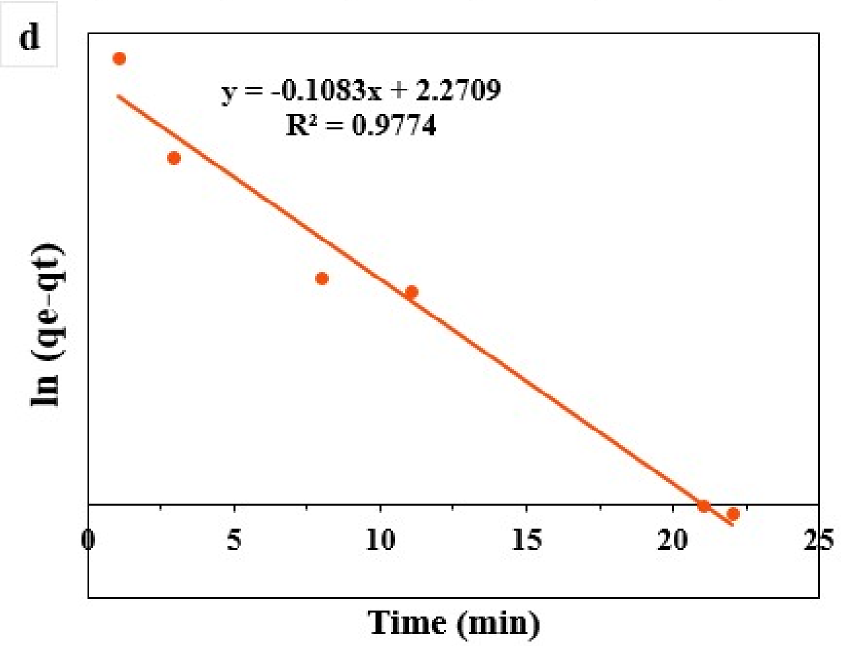
d
y = -0.1083x + 2.2709
R² = 0.9774
ln (qe-qt)
0
5
10
15
20
25
Time (min)

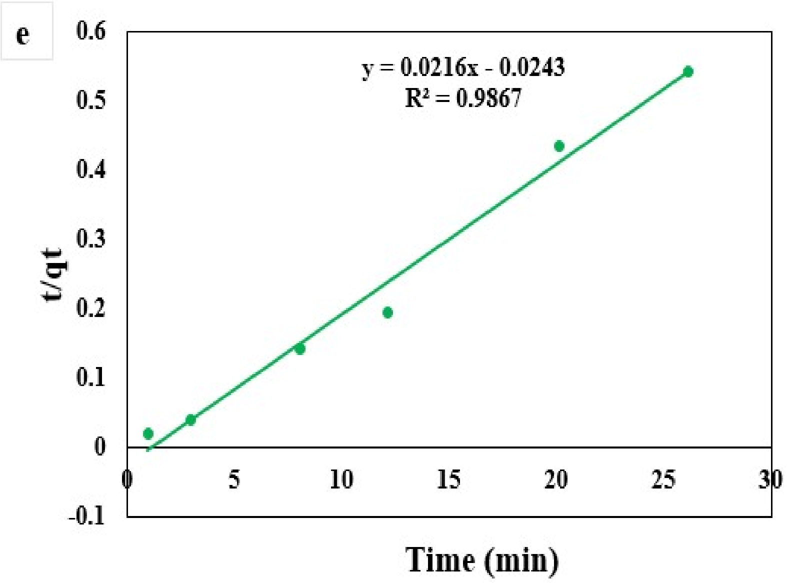
e
0.6
0.5
0.4
0.3
0.2
0.1
0
-0.1
t/qt
y = 0.0216x - 0.0243
R² = 0.9867
0
5
10
15
20
25
30
Time (min)

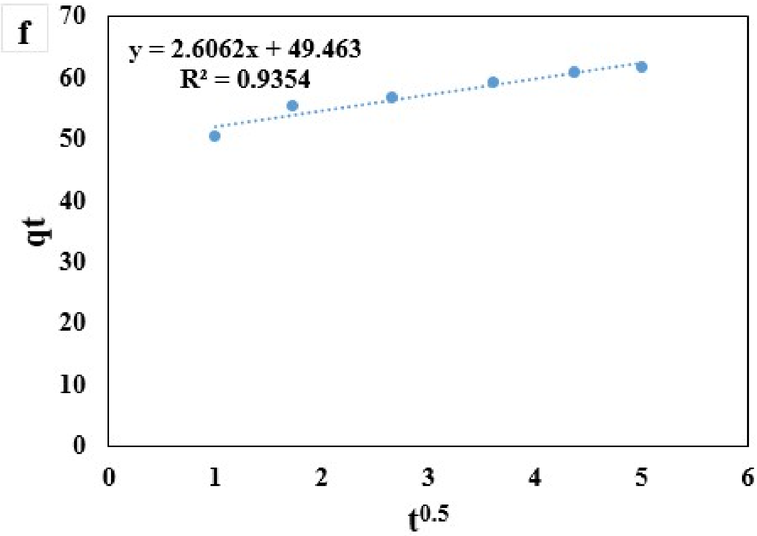

Fig.11: a) First order, b) Second order, c) Permeation model kinetics, d) Langmuir, e) Freundlich and f) Temkin isothermal diagram for EDTA F-MAC.

3.4. Reusability of process

To evaluate the reusability of the EDTA F-MAC adsorbent, the adsorption efficiency was tested over six consecutive cycles using a 0.5 M HCl solution under optimal conditions (pH ≈ 1, ambient temperature). As shown in **fig. 12**, the removal efficiency for Ni^{2+} decreased from 97.8% to 70.46% (a reduction of 27.34%), while MG removal declined from 98.04% to 87.31% (a reduction of 10.73%). These results demonstrate that the adsorbent retains a substantial portion of its performance over multiple cycles, indicating good regeneration capability. The sharper decline in Ni^{2+} efficiency may be attributed to partial detachment or degradation of EDTA functional groups during acid washing, which directly affects metal ion chelation. In contrast, MG adsorption relies more on electrostatic and π–π interactions, which are less sensitive to regeneration conditions. Overall, the EDTA F-MAC adsorbent exhibits high durability and practical reusability in repeated adsorption–desorption cycles [74, 75].

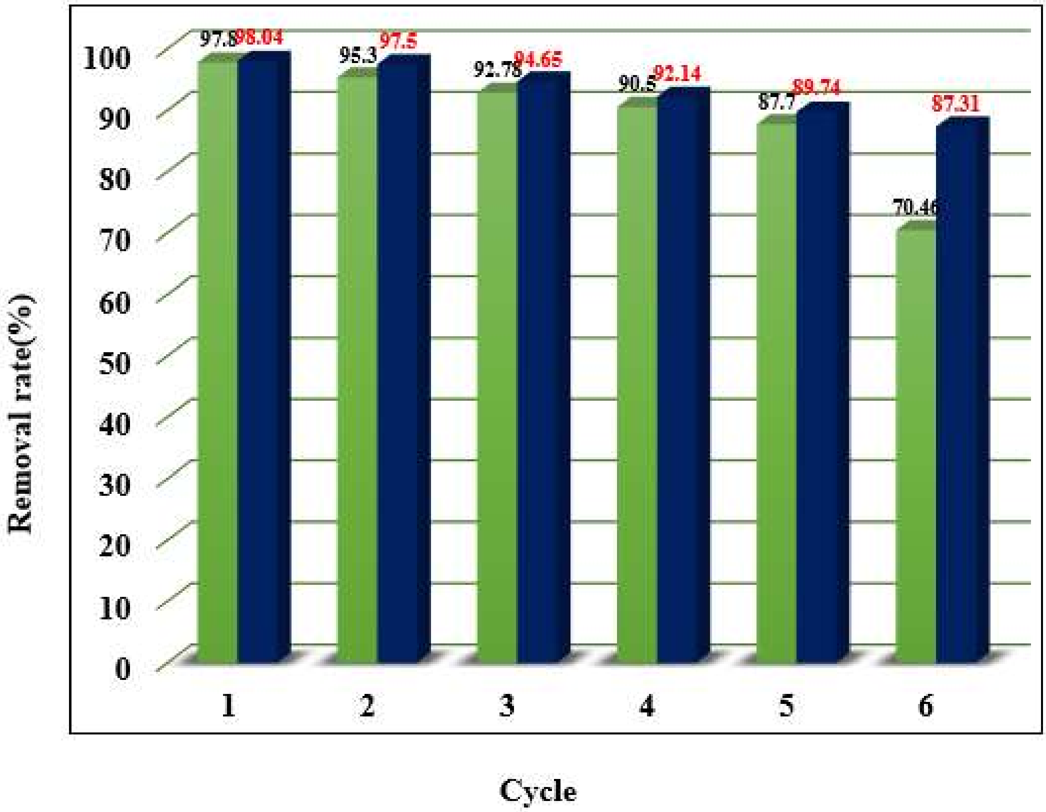

Fig 12. Repeatability of the process, for Ni^{2+} (green) and MG (blue) removal, in 6 consecutive cycles.

3.5. Limitations of the Study

Despite the promising performance of the developed EDTA-FMAC adsorbent, this study has certain limitations. All experiments were conducted under controlled laboratory conditions, which may not fully reflect the complexity of industrial wastewater systems. Moreover, the long-term structural stability of the adsorbent under continuous-flow operations and in multi-pollutant environments remains to be investigated. Future studies should address these aspects to better assess real-world applicability [76, 77].

4. Conclusion

This research focused on the production of activated carbon from sunflower stems, an agricultural waste material, for the removal of Ni^{2+} and MG from aqueous solutions. Activated carbon was synthesized, magnetized, and subsequently functionalized with EDTA. Structural and functional characterization using XRD, FT-IR, SEM, BET, and VSM confirmed the successful preparation of the EDTA-functionalized magnetic activated carbon. Adsorption experiments were conducted to evaluate the effects of pH, adsorbent dosage, contact time, and pollutant concentration. Under optimal conditions, the removal efficiency reached 94.63% for Ni^{2+} and 97.68% for MG. The experimental results showed strong agreement with the RSM model predictions, validating the reliability of the optimization approach. Despite these promising results, the study has certain limitations. All experiments were performed under controlled laboratory conditions, which may not fully reflect the complexity of industrial wastewater systems. Factors such as long-term structural stability, regeneration cost, and performance under continuous-flow and multi-pollutant environments remain to be investigated. These limitations highlight the need for further validation under real-world conditions. Nevertheless, the EDTA-FMAC adsorbent shows strong potential for industrial water treatment applications, particularly in the selective removal of heavy metals. Future research should focus on pilot-scale implementation, integration into existing treatment systems, and material optimization for enhanced selectivity and durability.

References

1. Zhang K., Luo X., Yang L., Chang Z., Luo S., (2021), Progress toward Hydrogels in Removing Heavy Metals from Water: Problems and Solutions—A Review. *ACS ES&T Water.* 1: 1098-116. https://doi.org/10.1021/acsomega.1c00999

2. Kothavale V.P., Sharma A., Dhavale R.P., Chavan V.D., Shingte S.R., Selyshchev O., et al., (2023), Carboxyl and thiol-functionalized magnetic nanoadsorbents for efficient and simultaneous removal of Pb(II), Cd(II), and Ni(II) heavy metal ions from aqueous solutions: Studies of adsorption, kinetics, and isotherms. *J. Phys. Chem. Solids.* 172: 111089. https://doi.org/10.1016/j.jpcs.2023.111089

3. Sulthana S.F., Iqbal U.M., Suseela S.B., Anbazhagan R., Chinthaginjala R., Chitathuru D., et al., (2024), Electrochemical Sensors for Heavy Metal Ion Detection in Aqueous Medium: A Systematic Review. *ACS Omega.* 9: 25493-512. https://doi.org/10.1021/acsomega.4c02765

4. Wang Z., Zhang L., Fang P., Wang L., Wang W., (2020), Study on Simultaneous Removal of Dye and Heavy Metal Ions by NiAl-Layered Double Hydroxide Films. *ACS Omega.* 5: 21805-14. https://doi.org/10.1021/acsomega.5b02740

5. ŞAhİN M., Atasoy M., Arslan Y., Yildiz D., (2023), Removal of Ni(II), Cu(II), Pb(II), and Cd(II) from Aqueous Phases by Silver Nanoparticles and Magnetic Nanoparticles/Nanocomposites. *ACS Omega*. 8: 34834-43. https://doi.org/10.1021/acsomega.8b04725

6. Sadjadi, M. S., Sadeghi, B., Zare, K. (2007). Natural bond orbital (NBO) population analysis of cyclic thionylphosphazenes, [NSOX $(NPCl_2)_2$]; X=F (1), X=Cl (2). *Journal of Molecular Structure: THEOCHEM*, 817(1–3), 27-33. https://doi.org/10.1016/j.theochem.2007.04.015

7. Dharmapriya T.N., Li D., Chung Y-C., Huang P-J., (2021), Green Synthesis of Reusable Adsorbents for the Removal of Heavy Metal Ions. ACS Omega. 6: 30478-87. https://doi.org/10.1021/acsomega.6c04350

8. Tripathi A., Ranjan M., (2015), Heavy Metal Removal from Wastewater Using Low Cost Adsorbents. *J. Bioremed. Biodeg.* 6: 315. https://doi.org/10.4172/2155-6199.1000315

9. Verma M., Lee I., Sharma S., Kumar R., Kumar V., Kim H., (2021), Simultaneous Removal of Heavy Metals and Ciprofloxacin Micropollutants from Wastewater Using Ethylenediaminetetraacetic Acid-Functionalized β-Cyclodextrin-Chitosan Adsorbent. *ACS Omega*. 6: 34624-34. https://doi.org/10.1021/acsomega.6c05420

10. Sadjadi, M. A. S., Meskinfam, M., Sadeghi, B., Jazdarreh, H., & Zare, K. (2011). In situ biomimetic synthesis and characterization of nano hydroxyapatite in gelatin matrix. *Journal of Biomedical Nanotechnology, 7*(3), 450-454. https://doi.org/10.1166/jbn.2011.1305

11. Garg R., Garg R., Okon Eddy N., Ibrahim Almohana A., Fahad Almojil S., Amir Khan M., et al., (2022), Biosynthesized silica-based zinc oxide nanocomposites for the sequestration of heavy metal ions from aqueous solutions. *J. King Saud Univ. Sci.* 34: 101996. https://doi.org/10.1016/j.jksus.2021.101996

12. Witkowska D., Słowik J., Chilicka K., (2021), Heavy Metals and Human Health: Possible Exposure Pathways and the Competition for Protein Binding Sites. *Molecules.* 26: 19. https://doi.org/10.3390/molecules26112345

13. El Hanandeh A., Mahdi Z., Imtiaz M.S., (2021), Modelling of the adsorption of Pb, Cu and Ni ions from single and multi-component aqueous solutions by date seed derived biochar: Comparison of six machine learning approaches. *Environ. Res.* 192: 110338. https://doi.org/10.1016/j.envres.2020.110338

14. Amininia, A., Pourshamsian, K., & Sadeghi, B. (2020). Nano-ZnO impregnated on starch—A highly efficient heterogeneous bio-based catalyst for one-pot synthesis of pyranopyrimidinone and xanthene derivatives as potential antibacterial agents. *Russian Journal of Organic Chemistry, 56*(7), 1279-1288. https://doi.org/10.1134/S1070428020070234

15. Muinde V.M., Onyari J.M., Wamalwa B., Wabomba J.N., (2020), Adsorption of malachite green dye from aqueous solutions using mesoporous chitosan–zinc oxide composite material. *Environ. Chem. Ecotoxicol.* 2: 115-25. https://doi.org/10.1016/j.enceco.2020.12.003

16. Sadeghi, B., Ghammamy, S., Gholipour, Z., Ghorchibeigy, M., & Amini Nia, A. (2011). Gold/hydroxypropyl cellulose hybrid nanocomposite constructed with more complete coverage of gold nano-shell. *Micro & Nano Letters*. https://doi.org/10.1016/j.theochem.2007.04.015

17. Sadeghy, B., & Ghammami, S. (2005). Oxidation of alcohols with tetramethylammonium fluorochromate in acetic acid. *Russian Journal of General Chemistry, 75*(12), 1886-1888. https://doi.org/10.1007/s11176-006-0008-0

18. Ali I., Burakova I., Galunin E., Burakov A., Mkrtchyan E., Melezhik A., et al., (2019), High-Speed and High-Capacity Removal of Methyl Orange and Malachite Green in Water Using Newly Developed Mesoporous Carbon: Kinetic and Isotherm Studies. *ACS Omega.* 4: 19293-306. https://doi.org/10.1021/acsomega.9c03013

19. Allah A.F., Abdel-Khalek A.A., El-Sherbeeny A.M., Al Zoubi W., Abukhadra M.R., (2023), Synthesis and Characterization of Iron-Rich Glauconite Nanorods by a Facile Sonochemical Method for Instantaneous and Eco-friendly Elimination of Malachite Green Dye from Aquatic Environments. *ACS Omega*. 8: 49347-61. https://doi.org/10.1021/acsomega.8c06157

20. Raval N.P., Shah P.U., Shah N.K., (2017), Malachite green “a cationic dye” and its removal from aqueous solution by adsorption. Appl. Water Sci. 7: 3407-45. https://doi.org/10.1007/s13201-017-0582-6

21. Chai W.S., Cheun J.Y., Kumar P.S., Mubashir M., Majeed Z., Banat F., et al., (2021), A review on conventional and novel materials towards heavy metal adsorption in wastewater treatment application. *J. Clean. Prod.* 296: 126589. https://doi.org/10.1016/j.jclepro.2021.126589

22. Daochalermwong A., Chanka N., Songsrirote K., Dittanet P., Niamnuy C., Seubsai A., (2020), Removal of Heavy Metal Ions Using Modified Celluloses Prepared from Pineapple Leaf Fiber. *ACS Omega*. 5: 5285-96. https://doi.org/10.1021/acsomega.9b03121

23. Pyrzynska K., (2019), Removal of cadmium from wastewaters with low-cost adsorbents. *J. Environ. Chem. Eng.* 7: 102795. https://doi.org/10.1016/j.jece.2018.11.036

24. Gupta A., Sharma V., Sharma K., Kumar V., Choudhary S., Mankotia P., et al., (2021), A Review of Adsorbents for Heavy Metal Decontamination: Growing Approach to Wastewater Treatment. *Mater.* 14: 16. https://doi.org/10.3390/ma14123456

25. Velusamy S., Roy A., Sundaram S., Kumar Mallick T., (2021), A Review on Heavy Metal Ions and Containing Dyes Removal Through Graphene Oxide-Based Adsorption Strategies for Textile Wastewater Treatment. *Chem. Rec.* 21: 1570-610. https://doi.org/10.1002/tcr.202100056

26. Darban Z., Shahabuddin S., Gaur R., Ahmad I., Sridewi N., (2022), Hydrogel-Based Adsorbent Material for the Effective Removal of Heavy Metals from Wastewater: A Comprehensive Review. *Gels.* 8: 5. https://doi.org/10.3390/gels8050225

27. Fouda-Mbanga B.G., Prabakaran E., Pillay K., (2021), Carbohydrate biopolymers, lignin based adsorbents for removal of heavy metals (Cd^{2+}, Pb^{2+}, Zn^{2+}) from wastewater, regeneration and reuse for spent adsorbents including latent fingerprint detection: A review. *Biotechnol. Rep.* 30: e00609. https://doi.org/10.1016/j.btre.2021.e00609

28. Duan C., Ma T., Wang J., Zhou Y., (2020), Removal of heavy metals from aqueous solution using carbon-based adsorbents: A review. *J. Water Process Eng.* 37: 101339. https://doi.org/10.1016/j.jwpe.2020.101339

29. Sultana M., Rownok M.H., Sabrin M., Rahaman M.H., Alam S.M.N., (2022), A review on experimental chemically modified activated carbon to enhance dye and heavy metals adsorption. *Clean. Eng. Technol.* 6: 100382. https://doi.org/10.1016/j.clet.2021.100382

30. Moosavi S., Lai C.W., Gan S., Zamiri G., Akbarzadeh Pivehzhani O., Johan M.R., (2020), Application of Efficient Magnetic Particles and Activated Carbon for Dye Removal from Wastewater. *ACS Omega.* 5: 20684-97. https://doi.org/10.1021/acsomega.0c03654

31. Lewoyehu M., (2021), Comprehensive review on synthesis and application of activated carbon from agricultural residues for the remediation of venomous pollutants in wastewater. *J. Anal. Appl. Pyrolysis.* 159: 105279. https://doi.org/10.1016/j.jaap.2020.105279

32. Moosavi S., Manta O., El-Badry Y.A., Hussein E.E., El-Bahy Z.M., Mohd Fawzi N.F., et al., (2021), A Study on Machine Learning Methods' Application for Dye Adsorption Prediction onto Agricultural Waste Activated Carbon. *Nanomater.* 11: 10. https://doi.org/10.3390/nano11101867

33. Nguyen D.T.C., Nguyen T.T., Le H.T.N., Nguyen T.T.T., Bach L.G., Nguyen T.D., et al., (2021), The sunflower plant family for bioenergy, environmental remediation, nanotechnology, medicine, food and agriculture: a review. *Environ. Chem. Lett.* 19: 3701-26. https://doi.org/10.1007/s10311-021-01213-5

34. Zubiolo C., de Santana H.E.P., Pereira L.L., Ruzene D.S., Silva D.P., Freitas L.S., (2024), Bio-Oil Production and Characterization from Corn Cob and Sunflower Stem Pyrolysis. *Ind. Eng. Chem. Res.* 63: 65-77. https://doi.org/10.1021/acs.iecr.4c03723

35. Anastopoulos I., Ighalo J.O., Adaobi Igwegbe C., Giannakoudakis D.A., Triantafyllidis K.S., Pashalidis I., et al., (2021), Sunflower-biomass derived adsorbents for toxic/heavy metals removal from (waste) water. *J. Mol. Liq.* 342: 117540. https://doi.org/10.1016/j.molliq.2021.117540

36. de Souza J.B., Michelin M., Amâncio F.L.R., Vital Brazil O.A., Polizeli M.d.L.T.M., Ruzene D.S., et al., (2020), Sunflower stalk as a carbon source inductive for fungal xylanase production. *Ind. Crops Prod.* 153: 112368. https://doi.org/10.1016/j.indcrop.2020.112368

37. Islam M., Islam M., Mittal H., Al Alili A., Alhassan S., (2023), Capturing water vapors from humid air using microporous activated carbon derived from sunflower seed shells. *Powder Technol.* 428: 118790. https://doi.org/10.1016/j.powtec.2023.118790

38. Abegunde S.M., Idowu K.S., Adejuwon O.M., Adeyemi-Adejolu T., (2020), A review on the influence of chemical modification on the performance of adsorbents. *Res. Environ. Sustain.* 1: 100001. https://doi.org/10.1016/j.resenv.2020.100001

39. Bhatnagar A., Hogland W., Marques M., Sillanpää M., (2013), An overview of the modification methods of activated carbon for its water treatment applications. *Chem. Eng. J.* 219: 499-511. https://doi.org/10.1016/j.cej.2012.12.103

40. Ambashta R.D., Sillanpää M., (2010), Water purification using magnetic assistance: A review. J. *Hazard. Mater.* 180: 38-49. https://doi.org/10.1016/j.jhazmat.2010.04.105

41. Reza M.S., Yun C.S., Afroze S., Radenahmad N., Bakar M.S.A., Saidur R., et al., (2020), Preparation of activated carbon from biomass and its applications in water and gas purification, a review. *Arab J. Basic Appl. Sci*. 27: 208-38. https://doi.org/10.1080/25765299.2020.1742242

42. Arora, Charu Kumar, Pramod Soni, Sanju Mittal, Jyoti Mittal, Alok Singh, Bhupender,(2020), Efficient removal of malachite green dye from aqueous solution using Curcuma caesia based activated carbon, Desalination and Water Treatment.195: 341-352. https://doi.org/10.5004/dwt.2020.25897.

43. Mittal, Alok,(2006), Adsorption kinetics of removal of a toxic dye, Malachite Green, from wastewater by using hen feathers, Journal of Hazardous Materials,133:196-202. https://doi.org/10.1016/j.jhazmat.2005.10.017.

44. Mittal, Alok Krishnan, Lisha Gupta, V. K,(2005), Removal and recovery of malachite green from wastewater using an agricultural waste material, de-oiled soya, Separation and Purification Technology,43: 125-133. https://doi.org/10.1016/j.seppur.2004.10.010

45. Gupta, V. K. Mittal, Alok Krishnan, Lisha Gajbe, Vibha,(2004), Adsorption kinetics and column operations for the removal and recovery of malachite green from wastewater using bottom ash, Separation and Purification Technology,40: 87-96. https://doi.org/10.1016/j.seppur.2004.01.008

46. Verma M., Lee I., Oh J., Kumar V., Kim H., (2022), Synthesis of EDTA-functionalized graphene oxide-chitosan nanocomposite for simultaneous removal of inorganic and organic pollutants from complex wastewater. *Chemosphere.* 287: 132385. https://doi.org/10.1016/j.chemosphere.2021.132385

47. Lian Z., Li Y., Xian H., Ouyang X-k., Lu Y., Peng X., et al., (2020), EDTA-functionalized magnetic chitosan oligosaccharide and carboxymethyl cellulose nanocomposite: Synthesis, characterization, and Pb(II) adsorption performance. Int. J. Biol. Macromol. 165: 591-600. https://doi.org/10.1016/j.ijbiomac.2020.09.204

48. Bhat S., Uthappa U.T., Sadhasivam T., Altalhi T., Soo Han S., Kurkuri M.D., (2023), Abundant cilantro derived high surface area activated carbon (AC) for superior adsorption performances of cationic/anionic dyes and supercapacitor application. Chem. Eng. J. 459: 141577.https://doi.org/10.1016/j.cej.2023.141577

49. Liu S., Yu B., Wang S., Shen Y., Cong H., (2020), Preparation, surface functionalization and application of Fe3O4 magnetic nanoparticles. Adv. Colloid Interface Sci. 281: 102165. https://doi.org/10.1016/j.cis.2020.10216

50. Wang X., Yun S., Fang W., Zhang C., Liang X., Lei Z., et al., (2018), Layer-Stacking Activated Carbon Derived from Sunflower Stalk as Electrode Materials for High-Performance Supercapacitors. ACS Sustain. Chem. Eng. 6: 11397-407. https://doi.org/10.1021/acssuschemeng.8b02163

51. Baysal M., Bilge K., Yılmaz B., Papila M., Yürüm Y., (2018), Preparation of high surface area activated carbon from waste-biomass of sunflower piths: Kinetics and equilibrium studies on the dye removal. J. Environ. Chem. Eng. 6: 1702-13. https://doi.org/10.1016/j.jece.2017.12.027

52. Sajjadi B., Shrestha R.M., Chen W-Y., Mattern D.L., Hammer N., Raman V., et al., (2021), Double-layer magnetized/functionalized biochar composite: Role of microporous structure for heavy metal removals. J. Water Process Eng. 39: 101677. https://doi.org/10.1016/j.jwpe.2020.101677
53. Barzegarzadeh M., Amini-Fazl M.S., (2023), Ultrasound-Assisted High-Performance Removal of Doxorubicin Using Functionalized Graphene Oxide-Fe3O4 Magnetic Nano-sorbent. J. Polym. Environ. 31: 177-92. https://doi.org/10.1007/s10924-022-02493-2
54. Zhang H., Li R., Zhang Z., (2022), A versatile EDTA and chitosan bi-functionalized magnetic bamboo biochar for simultaneous removal of methyl orange and heavy metals from complex wastewater. Environ. Pollut. 293: 118517. https://doi.org/10.1016/j.envpol.2021.118517
55. Wang R-s., Li Y., Shuai X-x., Liang R-h., Chen J., Liu C-m., (2021), Pectin/Activated Carbon-Based Porous Microsphere for Pb2+ Adsorption: Characterization and Adsorption Behaviour. Polym. 13: 15. https://doi.org/10.3390/polym13150200
56. Jiaming Z., LY L., Zhoub F., Mab H., Yanga K., Wu G., (2021), Synthesis and characterization of activated carbon from sugar beet residue for the adsorption of hexavalent chromium in aqueous solutions. R. Soc. Chem. 11: 8025-32. https://doi.org/10.1039/D0RA10954H
57. Ozpinar P., Dogan C., Demiral H., Morali U., Erol S., Samdan C., et al., (2022), Activated carbons prepared from hazelnut shell waste by phosphoric acid activation for supercapacitor electrode applications and comprehensive electrochemical analysis. Renew. Energy. 189: 535-48. https://doi.org/10.1016/j.renene.2021.12.007
58. Ebadollahzadeh H., Zabihi M., (2020), Competitive adsorption of methylene blue and Pb (II) ions on the nano-magnetic activated carbon and alumina. Mater. Chem. Phys. 248: 122893. https://doi.org/10.1016/j.matchemphys.2020.122893
59. Weaving J.S., Lim A., Millichamp J., Neville T.P., Ledwoch D., Kendrick E., et al., (2020), Elucidating the Sodiation Mechanism in Hard Carbon by Operando Raman Spectroscopy. ACS Appl. Energy Mater. 3: 7474-84. https://doi.org/10.1021/acsaem.0c01684
60. Madito M.J., (2021), Correlation of the Graphene Fermi-Level Shift and the Enhanced Electrochemical Performance of Graphene-Manganese Phosphate for Hybrid Supercapacitors: Raman Spectroscopy Analysis. ACS Appl. Mater. Interfaces. 13: 37014-26. https://doi.org/10.1021/acsami.1c08658
61. Jeskey J., Chen Y., Kim S., Xia Y., (2023), EDTA-Assisted Synthesis of Nitrogen-Doped Carbon Nanospheres with Uniform Sizes for Photonic and Electrocatalytic Applications. Chem. Mater. 35: 3024-32. https://doi.org/10.1021/acs.chemmater.3c00938
62. Paz R., Viltres H., Gupta N.K., Leyva C., (2021), Fabrication of magnetic cerium-organic framework-activated carbon composite for charged dye removal from aqueous solutions. J. Mol. Liq. 337: 116578. https://doi.org/10.1016/j.molliq.2021.116578
63. Duan Z., Zhang W., Lu M., Shao Z., Huang W., Li J., et al., (2020), Magnetic Fe3O4/activated carbon for combined adsorption and Fenton oxidation of 4-chlorophenol. Carbon. 167: 351-63. https://doi.org/10.1016/j.carbon.2020.05.070
64. Bora M., Benoy S.M., Tamuly J., Saikia B.K., (2021), Ultrasonic-assisted chemical synthesis of activated carbon from low-quality subbituminous coal and its preliminary evaluation towards supercapacitor applications. J. Environ. Chem. Eng. 9: 104986. https://doi.org/10.1016/j.jece.2020.104986
65. Islam M.N., Sarker J., Khatton A., Hossain S.M.M., Sikder H.A., Ahmed R., et al., (2022), Synthesis and characterization of activated carbon prepared from jute stick charcoal for industrial uses. Scholars Int. J. Chem. Mater. Sci. 5: 33-9. https://doi.org/10.36348/sijcms.2022.v05i03.001
66. Mahdiyeh Tajer M.A., Salehi S., (2020), Fabrication of polyacrylonitrile hybrid nanofiber scaffold containing activated carbon by electrospinning process as nanofilter media for SO2, CO2, and CH4 adsorption. Environ. Prog. Sustain. Energy. 40: 1. https://doi.org/10.1002/ep.13475

67. Qiu X., Wang S., Miao S., Suo H., Xu H., Hu Y., (2021), Co-immobilization of laccase and ABTS onto amino-functionalized ionic liquid-modified magnetic chitosan nanoparticles for pollutants removal. J. Hazard. Mater. 401: 123353. https://doi.org/10.1016/j.jhazmat.2020.123353
68. Waly S.M., El-Wakil A.M., El-Maaty W.M.A., Awad F.S., (2021), Efficient removal of Pb(II) and Hg(II) ions from aqueous solution by amine and thiol modified activated carbon. J. Saudi Chem. Soc. 25: 101296. https://doi.org/10.1016/j.jscs.2021.101296
69. Dilokekunakul W., Teerachawanwong P., Klomkliang N., Supasitmongkol S., Chaemchuen S., (2020), Effects of nitrogen and oxygen functional groups and pore width of activated carbon on carbon dioxide capture: Temperature dependence. Chem. Eng. J. 389: 124413. https://doi.org/10.1016/j.cej.2020.124413
70. Foroutan R., Peighambardoust S.J., Peighambardoust S.H., Pateiro M., Lorenzo J.M., (2021), Adsorption of Crystal Violet Dye Using Activated Carbon of Lemon Wood and Activated Carbon/Fe3O4 Magnetic Nanocomposite from Aqueous Solutions: A Kinetic, Equilibrium and Thermodynamic Study. Molecules. 26: 8. https://doi.org/10.3390/molecules26082345
71. Vinayagam R., Pai S., Murugesan G., Varadavenkatesan T., Narayanasamy S., Selvaraj R., (2022), Magnetic activated charcoal/Fe2O3 nanocomposite for the adsorptive removal of 2,4-Dichlorophenoxyacetic acid (2,4-D) from aqueous solutions: Synthesis, characterization, optimization, kinetic and isotherm studies. Chemosphere. 286: 131938 https://doi.org/10.1016/j.chemosphere.2021.131938
72. Takmil F., Esmaeili H., Mousavi S.M., Hashemi S.A., (2020), Nano-magnetically modified activated carbon prepared by oak shell for treatment of wastewater containing fluoride ion. Adv. Powder Technol. 31: 3236-45. https://doi.org/10.1016/j.apt.2020.06.017
73. Konicki W., Aleksandrzak M., Mijowska E., (2017), Equilibrium and kinetics studies for the adsorption of Ni and Fe ions from aqueous solution by graphene oxide. Pol. J. Chem. Technol. 19: 120-9. https://doi.org/10.1515/pjct-2017-0022
74. 74. Pourreza, T., Alijani, A., Arab Maleki, V., Kazemi, A. (2022). The effect of magnetic field on buckling and nonlinear vibrations of graphene nanosheets based on nonlocal elasticity theory. Iranian Journal of Nanoscience and Nanotechnology, Research Paper. https://doi.org/10.22034/IJND.2022.683988.
75. Amraee, A., Sarikhani, A., Rasaneh, S. (2024). The astonishing ultra-small iron oxide nanoparticles as positive contrast agents for MR imaging of cancerous tissues: A review. International Journal of Nano Dimension. https://doi.org/10.57647/j.ijnd.2024.1502.09.
76. Mokhtari, F., Poladian, M., Shamloo, A. (2023). A method for macromolecule transport to the spinal cord nervous system trauma with a combination of ultrasound and magnetic fields. International Journal of Nano Dimension, Research Paper. https://doi.org/10.22034/IJND.2023.1996487.2256.
77. Taleshi, F., Moradi, R., Sohrabi, L. (2023). Structure, magnetic, and optical properties of $NiFe_2O_4$ nanoparticle doped on the surface of carbon nanotube as a substrate. International Journal of Nano Dimension, Research Paper. https://doi.org/10.22034/IJND.2023.1998710.2272.